ISSN-1996-918X
Pak. J. Anal. Environ. Chem. Vol. 27, No. 1 (2026) 617696ap
http://doi.org/10.21743/pjaec/2026/617696ap

PVP-Directed MOF-Derived Fe–N–C Catalysts: Toward High-Performance and Sustainable PEM Fuel Cell Cathodes

Muhammad Shoaib[1], Shagufta Ishtiaque[1], Ahsan Abdul Ghani[1]*, Atif Zafar[2] and Abid Ali[3]

[1]Department of Chemical Engineering, University of Karachi, Karachi, Pakistan.
[2]Department of Petroleum Technology, University of Karachi, Karachi, Pakistan.
[3]Chongqing Key Laboratory for Advanced Materials and Technologies of Clean Energies, School of Materials and Energy, Southwest University, Chongqing 400715, PR China.
*Corresponding author Email:ahsan.ghani@uok.edu.pk

Received 22 August 2025, Revised 27 December 2025, Accepted 15 January 2026
Academic Editor: Huma Muddasar

Abstract

The urgent need to reduce carbon emissions and transition toward cleaner energy systems has intensified the search for electrocatalysts that are both efficient and resource-sustainable. Proton exchange membrane fuel cells (PEMFCs), powered by the oxygen reduction reaction (ORR), represent a key technology in this shift, but their reliance on platinum-group metals (PGMs) limits large-scale deployment. Single-atom Fe–N–C catalysts have emerged as promising PGM-free alternatives in acidic electrolytes, offering a balance of performance, cost, and environmental benefits. In this study, we report Fe-N-DPC-1000, an iron- and nitrogen-doped porous carbon synthesized at 1000 °C through a polyvinylpyrrolidone (PVP)-assisted metal–organic framework (MOF) strategy. The introduction of PVP during precursor formation promotes nitrogen incorporation, ensures atomic-level Fe dispersion, and stabilizes the framework during pyrolysis. The resulting material exhibits a hierarchical micro–mesoporous structure with a BET surface area ~ 1580 m^2g^{-1} along with a micropore volume of 0.54 cm^3g^{-1}. Single-cell PEMFC testing demonstrated a peak power density of 1205 $mWcm^{-2}$, approaching the level of Pt/C performance and outperforming its PVP-free counterpart by 35.3%, while maintaining strong stability. These results establish polymer-assisted MOF engineering as a scalable approach to designing high-performance Fe–N–C catalysts for next-generation, environmentally sustainable fuel cell technologies.

Keywords: Proton exchange membrane fuel cells (PEMFCs), Oxygen reduction reaction (ORR), Platinum-group-metal-free (PGM-free) catalysts, Fe–N–C catalysts, Sustainable energy conversion.

Introduction

The global shift toward cleaner, more sustainable, and low-carbon energy systems has been gathering tremendous pace in recent years. This change is largely fueled by growing public and scientific concern over the escalating impacts of climate change, depletion of fossil fuel reserves, and the urgent global call to curb greenhouse gas emissions. So, there is an increasing emphasis on developing efficient, renewable, and carbon-neutral technologies. Among the various emerging alternatives, proton exchange membrane fuel cells (PEMFCs) are known as one of the most promising solutions. These systems can convert hydrogen directly into electricity through an electrochemical process that emits only water as a byproduct, offering a clean and efficient pathway toward

a truly sustainable energy future [1, 2]. They also provide high energy density, rapid startup, and reliable operation at moderate temperatures, making them attractive for use in transportation, stationary power, and portable applications [2, 3]. Nevertheless, the widespread commercialization of PEMFCs has been constrained by their dependence on platinum-group metals (PGMs), particularly platinum, as catalysts for the oxygen reduction reaction (ORR) at the cathode [4, 5]. The limited availability, high cost, and supply risks associated with PGMs remain major barriers to cost-competitive and sustainable fuel cell systems [6, 7]. This challenge has spurred extensive efforts to design catalysts that do not rely on PGMs [4, 8, 9]. In particular, atomically dispersed Fe species coordinated with nitrogen (Fe–N_x sites) have been reported to achieve ORR activity in acidic electrolytes comparable to that of platinum [10, 11]. Beyond their strong intrinsic activity, Fe–N–C catalysts are attractive due to their low cost, earth-abundant precursors, and compatibility with current PEMFC configurations. However, limitations in durability, active site density, and mass transport continue to hinder their commercialization [12, 13].

The ORR performance of Fe–N–C catalysts is strongly influenced by their structural and compositional characteristics [3, 14]. Maximizing the density of Fe–N_x sites requires maintaining atomic dispersion of Fe while suppressing the formation of metallic nanoparticles, which not only diminishes activity but also dissolves readily under acidic conditions [15, 16]. Porosity is another critical parameter: micropores provide anchoring sites for Fe–N_x centers, whereas mesopores facilitate oxygen and proton transport and help remove product water [17, 18]. A carefully engineered micro–mesoporous architecture is therefore regarded as essential for high catalytic activity and optimal utilization of active sites [17, 19]. Yet, constructing such hierarchically integrated structures remains challenging. Metal–organic frameworks (MOFs) have recently attracted significant attention as precursors for Fe–N–C catalysts, owing to their large surface areas, uniform distribution of metal and nitrogen atoms, and tunable chemical environments [20–22]. Among them, zeolitic imidazolate frameworks (ZIFs), particularly ZIF-8, are the most widely used because of their simple synthesis, structural robustness, and inherent microporosity [23–25]. Upon pyrolysis, these frameworks transform into nitrogen-doped porous carbon matrices that effectively anchor and disperse Fe species [26, 27]. Despite these advantages, MOF-derived Fe–N–C catalysts also face drawbacks: high-temperature treatment can partially collapse the framework, reduce microporosity, and promote uncontrolled Fe particle aggregation, all of which impair catalytic activity and durability [3, 5, 13, 28].

To overcome these challenges, several approaches have been explored, including the introduction of secondary nitrogen sources, the design of bimetallic systems, and the use of templating methods to control porosity [29–34]. More recently, attention has shifted to incorporating polymer additives as a promising strategy. Incorporated during MOF precursor synthesis, polymers can serve as structure-directing agents, stabilizers, or dopants. In this role, they affect the distribution of metal ions, help maintain the framework during pyrolysis, and enrich the final carbon with nitrogen functionalities [35–38]. Among the various options, polyvinylpyrrolidone (PVP) has attracted particular interest because it binds strongly with transition-metal ions, supplies nitrogen upon pyrolysis, and prevents sintering of particles at elevated temperatures

[24, 39, 40]. These attributes suggest that PVP could be highly effective in enhancing the structural integrity and catalytic activity of MOF-derived Fe–N–C systems. Yet, its use as a deliberate directing agent in synthesizing Fe–N–C catalysts for PEMFC applications has not been systematically examined.

This gap is significant, since the multifunctional role of PVP could directly address key limitations in Fe–N–C catalyst development. Through enhanced nitrogen incorporation, stabilization of the MOF crystal framework, and promotion of atomic-level Fe dispersion, PVP-assisted synthesis offers a promising route to catalysts with both high active-site density and well-preserved microporous channels [24, 26, 36, 41]. To fully establish its potential, however, a systematic investigation is required to assess not only the effectiveness of this method but also its scalability for practical PEMFC applications. In this work, we introduce a PVP-assisted MOF strategy for preparing Fe-N-DPC-1000, a hierarchically porous Fe–N–C catalyst designed for oxygen reduction in acidic fuel cells. Incorporation of PVP during MOF precursor formation modifies the carbonization pathway, leading to preserved microporosity, enhanced nitrogen coordination, and atomically dispersed Fe species without detectable nanoparticle formation. These structural advantages translate into notably enhanced fuel cell performance, with Fe-N-DPC-1000 reaching a peak power density of 1205 $mWcm^{-2}$, approaching the benchmark of commercial Pt/C under identical conditions. Importantly, the introduction of PVP during synthesis enhances the power density by nearly 35.3% compared with the non-PVP analogue. This PVP-assisted MOF strategy offers a scalable and environmentally sustainable pathway toward platinum-free ORR catalysts, supporting the advancement of durable, cost-effective PEMFC systems as part of the global transition to a low-carbon energy future.

Materials and Methods

Chemicals and Reagents

All chemicals used in this work were of analytical grade and were employed without any further purification. The organic linker 2-methylimidazole (2-MeIm, $C_4H_6N_2$, ≥99%) and zinc nitrate hexahydrate ($Zn(NO_3)_2·6H_2O$, ≥99%) were purchased from Sigma-Aldrich and used as the starting precursors for the formation of ZIF-8. Iron(III) nitrate nonahydrate ($Fe(NO_3)_3·9H_2O$, ≥98%), also obtained from Sigma-Aldrich, served as the source of iron for the Fe–N–C catalysts. Polyvinylpyrrolidone (PVP, Mw ≈ 10,000) was employed as a polymeric additive to regulate crystal growth during MOF formation and to contribute nitrogen functionalities during subsequent pyrolysis.

For electrode and MEA preparation, Nafion® ionomer (5 wt% dispersion, D2020) was purchased from Alfa Aesar and used as the proton-conducting binder in catalyst inks. Sulfuric acid (H_2SO_4, 98%) from Alfa Aesar was used as the electrolyte for electrochemical tests in acidic media. Solvents including methanol, ethanol, and isopropanol were of analytical grade and were obtained from local suppliers. Ultrapure water with a resistivity greater than 18.2 MΩ·cm was employed in all solution preparations and washing steps to ensure purity.

High-purity gases were used throughout the experimental work. Oxygen (99.999%), nitrogen (99.9999%), and hydrogen (99.999%) were supplied in compressed cylinders; compressed air was used for PEMFC single-cell testing. These specifications align with standard practice in

catalyst synthesis and electrochemical evaluation and help ensure that results are not confounded by impurities or reagent variability.

Catalyst Synthesis

The preparation of the Fe–N–C electrocatalyst was carried out through a PVP-mediated MOF method, following our previous method [42]. To prepare the sample, 2-methylimidazole (MeIm, $C_4H_6N_2$) having mass of 1 g was first dissolved in 62.5 mL of methanol, forming what was designated as solution A. Into this mixture, 0.3125 g of PVP was introduced and stirred until the solution became completely clear. Meanwhile, another mixture—referred to as solution B—was made by dissolving 0.6 g of zinc nitrate hexahydrate ($Zn(NO_3)_2 \cdot 6H_2O$) along with 0.026 g of iron(III) nitrate nonahydrate ($Fe(NO_3)_3 \cdot 9H_2O$) in an equal volume (62.5 mL) of methanol. Afterwards, solution B was then poured into solution A while mixing vigorously, resulting in immediate nucleation of PVP-stabilized Fe-incorporated ZIF-8 crystals. The resulting mixture was kept under continuous stirring at room temperature for 12 h, allowing for complete crystal growth.

The crystals were recovered by centrifugation at 7200 rpm for 10 min, rinsed three times with ethanol to eliminate residual precursors, and dried under vacuum at 60 °C for 8 h. The dry precursor was then carbonized in a tube furnace under flowing nitrogen, where the temperature was ramped to 1000 °C at a heating rate of 5 °C per min and maintained for 2 h. The resulting porous carbon material, with iron and nitrogen functionalities, was designated Fe-N-DPC-1000. To provide a reference, a second sample was synthesized under identical conditions but without the addition of PVP, referred to as Fe-N-C-1000.

Structural and Compositional Analysis

To evaluate the physicochemical properties of the synthesized catalysts, multiple characterization techniques were employed. X-ray diffraction (XRD) patterns were recorded on a PANalytical X'Pert PRO diffractometer using Cu Kα radiation (λ = 1.5406 Å). The patterns were measured over a 2θ range of 10–80° with a scan rate of 4° min^{-1}. The surface and bulk morphologies were characterized by electron microscopy. (SEM) images were obtained with a Zeiss Ultra55 operating at 5 kV, whereas high-resolution % Transmission Electron Microscopy (TEM) pictures were carried out on a Hitachi H-9500 at 300 kV. Textural properties, including the specific surface area and porosity were analyzed through N_2 adsorption–desorption measurements conducted at 77 K, measured on a Quantachrome Autosorb-1-C analyzer. All specimens were degassed at 473 K for 2 h prior to measurement. The pore size distribution was further evaluated using BET, DR, and DFT models. PHI-5000C was used for the surface chemistry determination by X-ray photoelectron spectroscopy (XPS) with Mg Kα radiation. Spectral fitting and quantification were performed using XPS Peak 4.1 software. Finally, the total Fe content was measured by ICP-OES (Agilent 5900) after complete acid digestion of the catalyst powders.

Electrochemical Evaluation Under PEMFC Conditions

MEA fabrication and cell assembly

To assess their functionality in fuel cell operation, the catalysts were incorporated into membrane electrode assemblies (MEAs) and tested under PEMFC conditions, in line with best practices for platinum-group-metal-free cathodes [43]. Catalyst inks were formulated by sonicating a mixture of 10 mg

of the synthesized catalyst, 200 mg of 5 wt% Nafion solution, 0.50 mL of isopropanol, and 0.25 mL of deionized water. The homogeneous ink was applied onto carbon paper substrates, producing cathodes with a catalyst loading of 3.0 mg cm^{-2}. The anode side was prepared using a commercial platinum-on-carbon catalyst (28.6 wt% Pt), with a Pt loading of 0.10 mg cm^{-2}. Both electrodes were combined with a Nafion 212 proton-conducting membrane by hot pressing under 0.6 MPa pressure at 130 °C for 120 sec. The resulting MEA was mounted into a single-cell PEMFC test fixture. Electrochemical measurements were conducted on an Arbin testing system at 80 °C using fully humidified reactant gases supplied under the designated back pressure. During operation, hydrogen was continuously supplied to the anode, whereas oxygen or air was introduced to the cathode, each at a controlled flow rate of 300 standard cubic centimeters per minute, ensuring smooth and balanced fuel cell operation [44, 45].

Operational testing

After assembly, the MEAs were gently conditioned to reach stable operating behavior before performance testing. The electrochemical activity was then examined by recording polarization curves using either H_2–air or H_2–O_2 as the reactant gases. All tests were carried out in a PEMFC setup at 80 °C under 2 bar back pressure and 100% relative humidity to closely simulate realistic operating conditions [46]. Voltage–current (V–I) curves and corresponding power density profiles were obtained by gradually increasing the current and monitoring the resulting cell voltage. This procedure made it possible to clearly distinguish between kinetic, ohmic, and mass-transport losses, offering a detailed understanding of fuel cell performance under practical working environments.

Results and Discussion

Morphological and Microscopic Characteristics

Electron microscopy offered the first insights into how the synthesis route affected particle morphology and nanoscale features. SEM images (Fig. 1a and 1b) show that Fe-N-DPC-1000 retains the clean, faceted polyhedral shape of the parent ZIF-8 crystals [22,47]. The particles retain flat faces and sharp corners even after treatment at 1000 °C, pointing to the "scaffold" role of PVP, which helps control shrinkage and prevents necking during carbonization [24,39]. In contrast, the PVP-free sample (Fe-N-C-1000) maintains only a rough polyhedral outline, with uneven surfaces, partial fusion at contact points, and greater variability in particle shape — features that suggest local sintering when the framework lacks polymer stabilization [34,41].

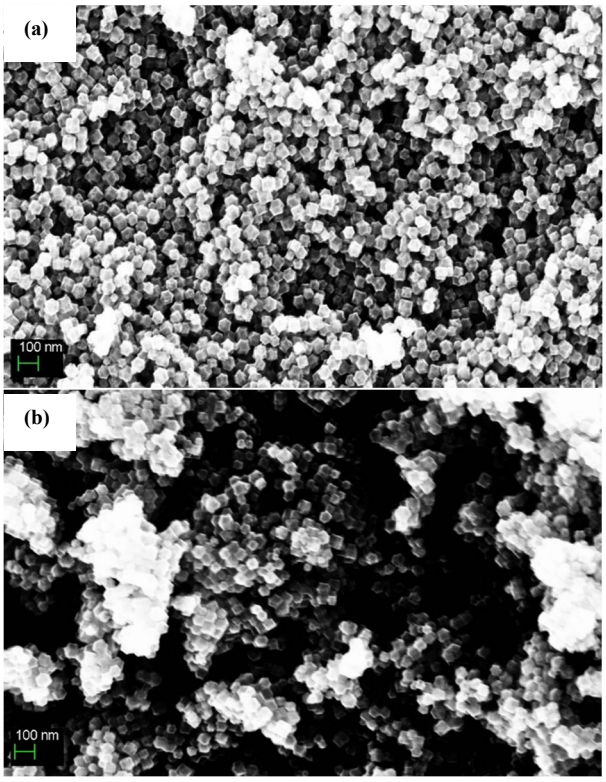

Figure 1. **SEM images of (a) Fe-N-DPC-1000 and (b) Fe-N-C-1000**

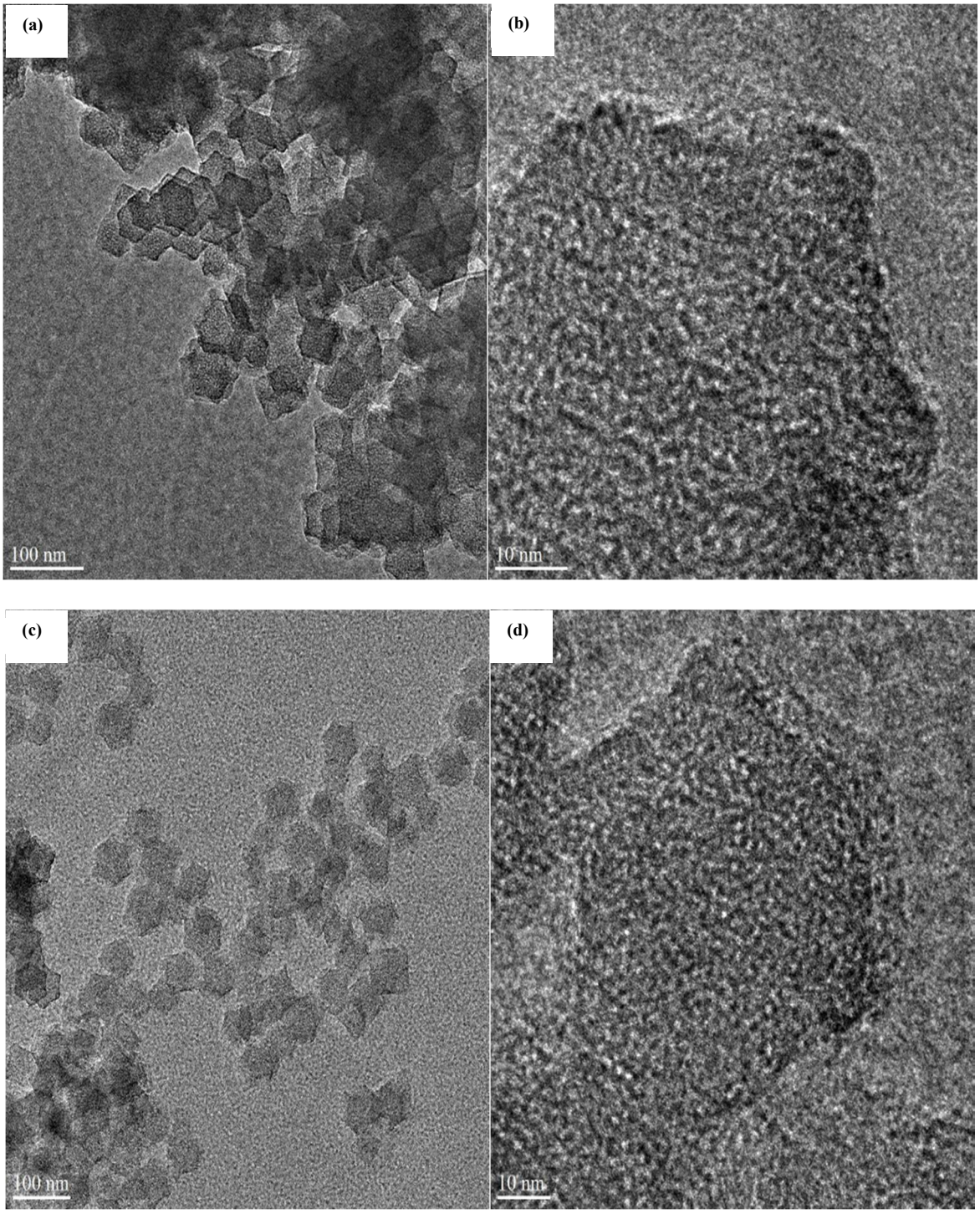

Figure 2. **(a – b) TEM and HRTEM images of Fe-N-DPC-1000, (c – d) TEM and HRTEM images of Fe-N-C-1000**

TEM further refines these observations (Fig. 2a and 2c). Both materials remain in the 50–60 nm size range, yet Fe-N-DPC-1000 exhibits uniform internal contrast and sharply defined boundaries, suggesting even porosity and an absence of dense Fe-rich pockets. High-resolution TEM (Fig. 2b and 2d) reveals largely amorphous carbon in both catalysts; no lattice fringes attributable to metallic Fe, Fe_3C, or Fe oxides are visible [48]. In Fe-N-DPC-

1000, bright, point-like spots are evenly dispersed throughout the carbon matrix, a hallmark of isolated Fe centers [49]. By contrast, Fe-N-C-1000 occasionally shows clusters of bright speckles, indicative of localized metal accumulation [24]. The PVP-enabled route therefore produces a more homogeneous distribution of atomically dispersed Fe-an essential prerequisite for maximizing the density and accessibility of Fe–N_x sites.

Elemental Distribution and Atomic Dispersion

To get a clearer picture of how the elements are distributed and whether the iron is incorporated evenly, we employed HAADF-STEM imaging along with Energy Dispersive X-ray (EDX) mapping for the Fe-N-DPC-1000 catalyst as shown in Fig. 3. The HAADF-STEM images display particles characterized by smooth contours and a uniform intensity pattern, suggesting a consistent mass–thickness distribution throughout the material. Corresponding EDX elemental maps indicate that nitrogen is not only present in greater amounts but also homogeneously distributed. The Fe signal aligns closely with both N and C regions, implying a profoundly dispersed arrangement of Fe species and excellent Fe–N_x coordination. The lack of Fe-rich agglomerates further supports the idea that PVP acts as a stabilizing agent, preserving isolated Fe atoms or small clusters during the pyrolysis process and preventing their aggregation.

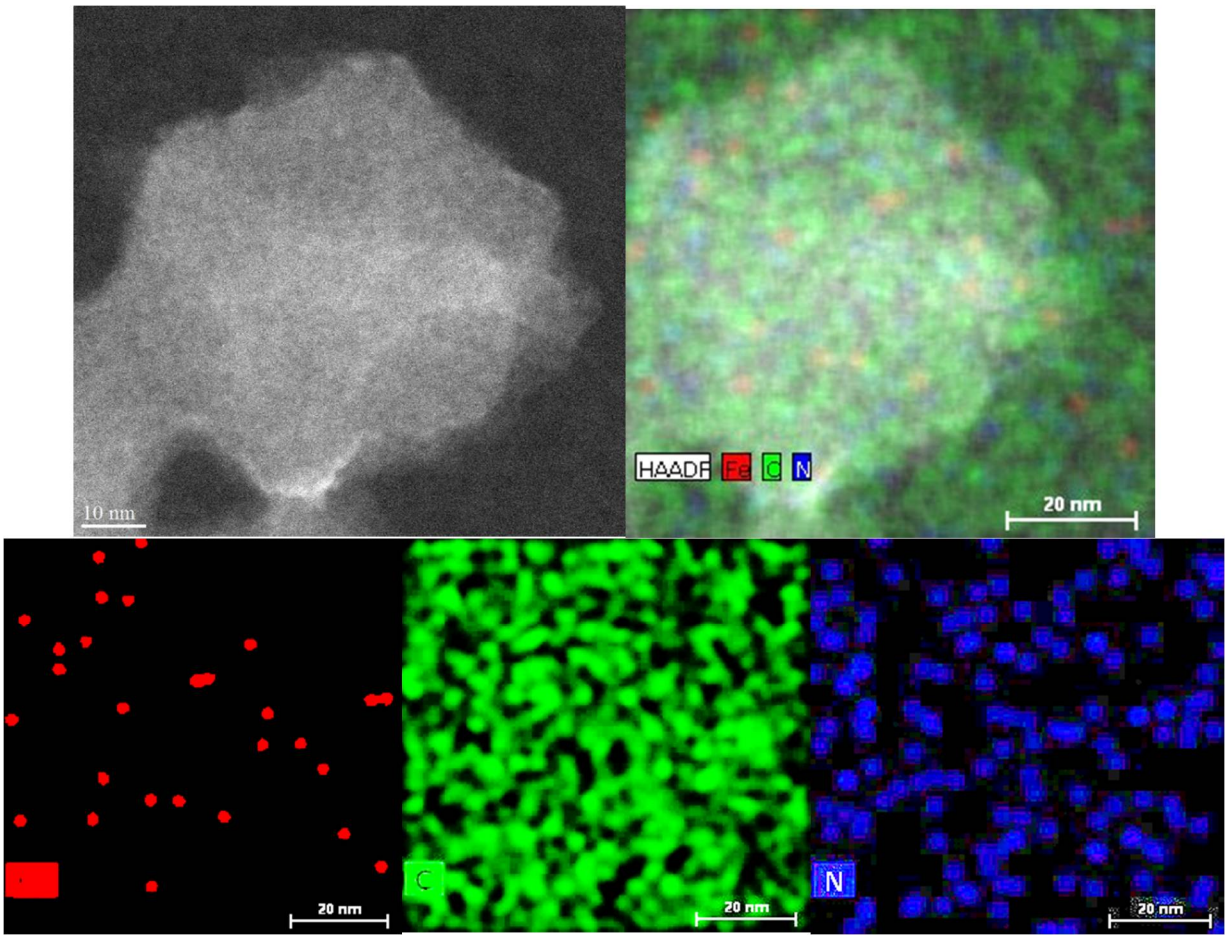

Figure 3. **HAADF-STEM image and corresponding EDX elemental mappings of Fe-N-DPC-1000.**

Structural and Compositional Features

To complement the microscopy and elemental mapping, we analyzed the bulk structure and composition using XRD and XPS. Powder XRD (Fig. 4) of the precursors shows the diagnostic ZIF-8 reflections at 2θ ≈ 10.3°, 12.7°, 14.6°, 16.4°, 18.0°, 22.1°, 24.6°, 26.7°, and 29.7°, in excellent agreement with the sodalite-type ZIF-8 reference, indexed to (002), (112), (022), (013), (222), (114), (233), (134), and (044), respectively [50–53]. These matches confirm correct framework formation and high crystallinity prior to pyrolysis. Additional weak features above 30° (31.6, 34.1, 34.98, 36.62, 38.92, 39.62, 44.7, 47.87, 56.3°) lack corroborating companion reflections (e.g., ZnO ≈ 62.9°, 66.4°; Zn ≈ 43.3°, 54.3°; α-Fe ≈ 65.0°, 82.3°); therefore, we make no assignments beyond ZIF-8 and regard all other features as absent or at most trace. No Bragg peaks of crystalline Fe (metallic Fe, Fe oxides, or Fe_3C) are detected in any of the patterns; Fe is thus inferred to be atomically dispersed or in amorphous domains [54,55], consistent with HRTEM observations. After pyrolysis, both catalysts exhibit a broad feature at 2θ ≈ 25°, assignable to the turbostratic-carbon (002) reflection [56], indicating high-temperature carbonization of Fe-N-C-1000 and Fe-N-DPC-1000.

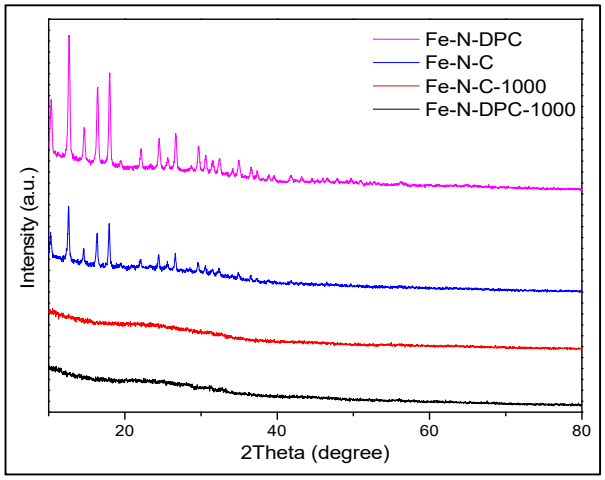

Figure 4. **XRD patterns of Fe–N–DPC-1000 and Fe–N–C-1000 before and after heat treatment**

XPS survey spectra (Fig. 5a) register C 1s, N 1s, O 1s, and Fe 2p signals for both samples [15, 57, 58]. Elemental analysis derived from XPS (Fig. 5b) shows that Fe-N-DPC-1000 carries higher nitrogen content but slightly lower total Fe than Fe-N-C-1000, while carbon remains comparable. This compositional shift reflects the dual role of PVP during precursor synthesis and pyrolysis: it not only introduces nitrogen but also coordinates Fe, thereby limiting excessive Fe incorporation and suppressing aggregation. From a catalytic perspective, this balance is crucial.

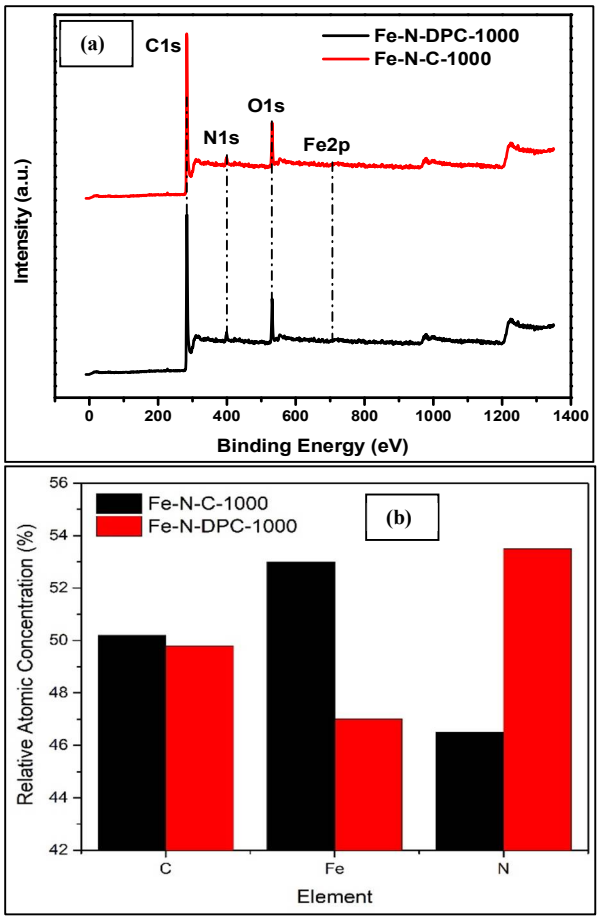

Figure 5. **(a) XPS spectrum profiles of Fe-N-DPC-1000 and Fe-N-C-1000, and (b) comparison of their relative atomic distributions as determined by XPS**

Enriching the nitrogen content while moderating Fe loading promotes the generation of $Fe–N_x$ moieties and minimizes

the formation of inactive metallic Fe domains, which are prone to dissolution or parasitic reactions in acidic PEMFC environments [24,54]. In essence, PVP-assisted synthesis directs the chemistry toward a higher proportion of catalytically active Fe–N_x centers embedded in a stable carbon framework.

Textural Properties and Pore Architecture

Nitrogen adsorption–desorption measurements (Fig. 6a) reveal clear differences in porosity and surface area between the two samples. Fe-N-DPC-1000 shows a rapid adsorption uptake in the low relative pressures region ($P/P_0 < 0.1$), characteristic of Type I isotherms, together with a modest hysteresis loop at higher pressures, features that point to a hierarchical micro–mesoporous structure [59, 60]. The Fe-N-C-1000 sample, on the other hand, exhibits a noticeably broader isotherm with strong hysteresis and only a weak feature in the low-pressure region, implying that its pore structure is dominated by mesopores while micropores are scarce [26,60].

BET analysis underscores the benefit of the PVP-assisted synthesis. Fe-N-DPC-1000 achieves a specific surface area of 1580 $m^2\ g^{-1}$, far exceeding the 177.3 $m^2\ g^{-1}$ of Fe-N-C-1000. Micropore volume determined by the DR method is 0.642 $cm^3\ g^{-1}$, more than nine times higher than the corresponding 0.077 $cm^3\ g^{-1}$ measured for the control. Pore-size distributions derived from DFT analysis (Figure 6b) confirm this contrast: Fe-N-DPC-1000 exhibits a dominant micropore mode at ~0.55 nm together with mesopores centered near 3.8 nm, while Fe-N-C-1000 shows a broader pore width mode at ~14.6 nm, consistent with framework collapse and pore coarsening.

These differences in pore structure have clear consequences for catalytic performance. In Fe-N-DPC-1000, micropores expose abundant Fe–N_x active sites, while mesopores act as diffusion channels for oxygen and facilitate the removal of water generated during operation [17,19,47]. Such a hierarchical pore system is especially advantageous at high current densities, where oxygen transport resistance and water accumulation often limit fuel cell output [34, 61]. The Fe-N-DPC-1000 combines high site density with efficient mass transport, whereas the PVP-free counterpart, with its weak microporosity and oversized mesopores, cannot achieve the same balance. These structural shortcomings anticipate the performance gap observed in device-level testing.

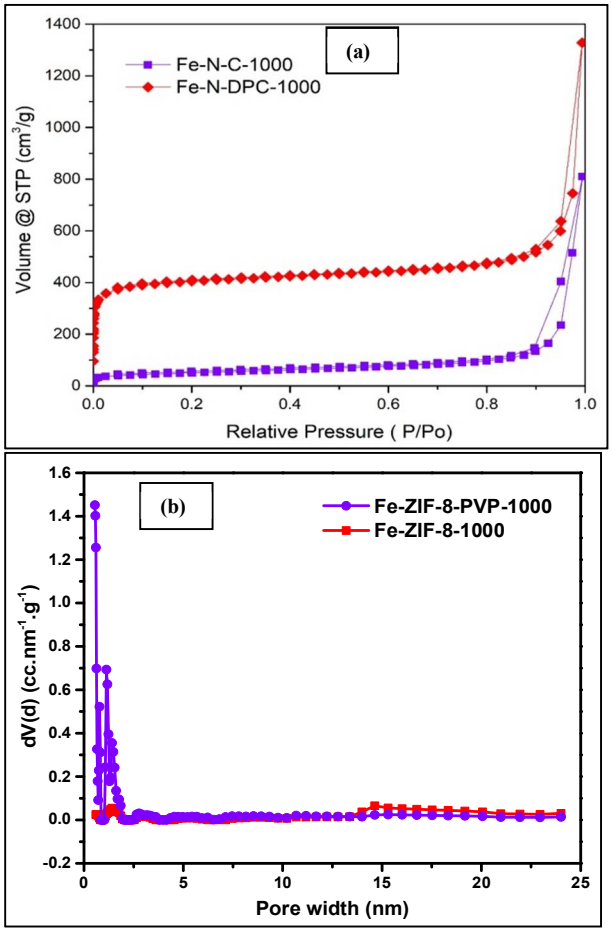

Figure 6. **(a) Nitrogen adsorption–desorption curves obtained for Fe-N-DPC-1000 and Fe-N-C-1000; (b) DFT distribution of pore sizes for the catalysts Fe-N-DPC-1000 and Fe-N-C-1000 with emphasis on micropore region**

Fuel Cell Performance

To assess the practical applicability of the catalysts, Fe-N-DPC-1000 and Fe-N-C-1000 were incorporated as cathodes in MEAs, with commercial Pt/C serving as the benchmark. Fig. 7 and 8 display the polarization and power density curves under both H_2–O_2 and H_2–air conditions at backpressures of 1 bar and 2 bar. The cathode loading was fixed at 3 mg cm^{-2}, with a Pt/C anode loading of 0.1 mg cm^{-2}.

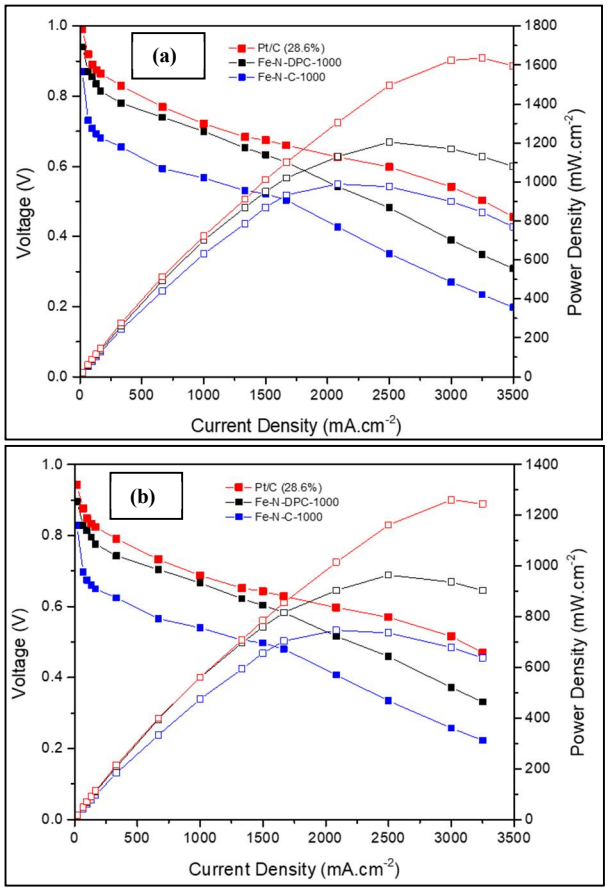

Figure 7. **H_2 - O_2 polarization test for fuel cell at a loading of 3 mg cm^{-2} of Fe-N-DPC-1000 / Fe-N-C-1000 / Pt/C and 0.1 mg cm^{-2} of Pt/C in cathode and anode, respectively at a pressure of (a) 2 bar (b) 1 bar**

Under H_2–O_2 operation at 2 bar (Fig. 7a), Fe-N-DPC-1000 achieved a peak power density of 1205 mW cm^{-2}, far exceeding the performance of Fe-N-C-1000 and approaching the level of Pt/C. At 1 bar (Fig. 7b), the peak output of Fe-N-DPC-1000 decreased as expected due to lower oxygen availability, yet it still delivered significantly higher performance than Fe-N-C-1000 and remained competitive with Pt/C. These results confirm that the incorporation of PVP during synthesis yields a catalyst that translates half-cell activity gains into meaningful single-cell performance improvements.

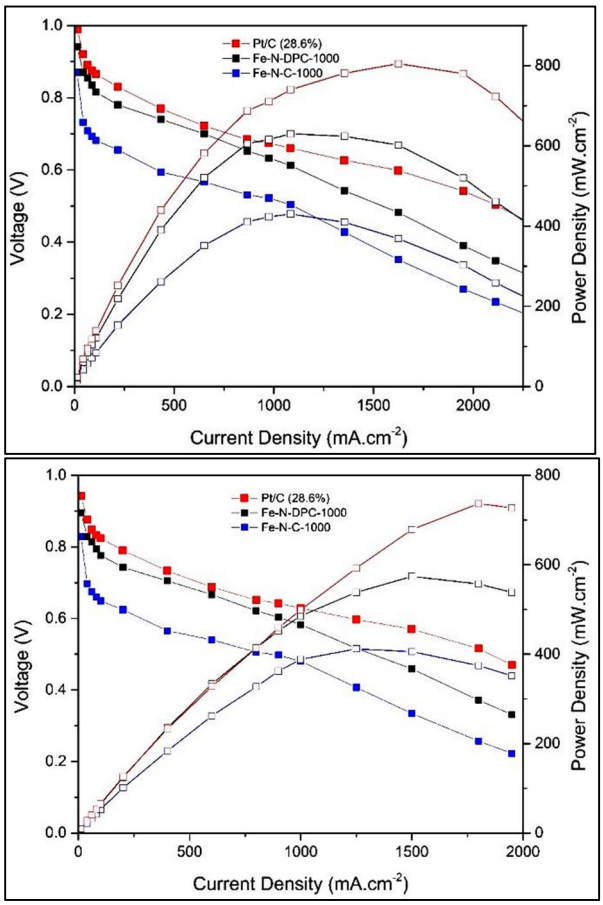

Figure 8. **H_2 - Air polarization test for fuel cell at a loading of 3 mg cm^{-2} Fe-N-DPC-1000 / Fe-N-C-1000 / Pt/C and 0.1 mg cm^{-2} of Pt/C in cathode and anode, respectively at a pressure of (a) 2 bar (b) 1 bar**

The same performance hierarchy was observed under H_2–air operation (Fig. 8). At 2 bar (Fig. 8a), Fe-N-DPC-1000 reached a peak power density of 708 mW cm^{-2}, whereas Fe-N-C-1000 performed substantially worse. At 1 bar (Fig. 8b), the PVP-assisted catalyst still achieved 420 mW cm^{-2}, confirming its ability to sustain activity under the more challenging

air feed, though with stronger mass-transport limitations. In both cases, Fe-N-DPC-1000 maintained a clear advantage over Fe-N-C-1000 and remained comparable to Pt/C under identical conditions.This is a remarkable result for a PGM-free catalyst in acidic media [3, 5, 44, 46, 62–64] and puts it among the top-performing PGM-free catalysts, as shown in Table 1. The advantage of the PVP-assisted route is clear: its peak power density is 35.3% greater than that of Fe-N-C-1000. This enhancement may be explained by the following main factors:

Table 1. **A comparison of the H_2/O_2 performance test of advanced and up-to-date PGM-free catalysts.**

Catalysts	T(°C)/ Relative Humidity (RH)	Back pressure	Catalyst Loading	Peak Power Density (W cm−2) Under O_2	Ref
Fe-N-DPC-1000	80 °C, 100% RH	2.00 bar for H_2 and O_2	Cathode loaded with 3.00 mg cat cm^{-2} and anode with 0.10 mg Pt cm^{-2}	1.205	This work
Fe/N/C(4mlm)-Oac	80 °C, 100% RH	1.00 bar	3.00 mg cat cm^{-2} on cathode with 0.40 mg Pt cm^{-2} on anode	1.18 (1.00 bar)	[14]
		2.00 bar	-	1.33 (2.00 bar)	
Fe–S–NC/Fe3C	70 °C	1.00 bar	Cathode loaded with 3.00 mg cat cm^{-2}; anode loaded with 0.10 mg Pt cm^{-2}	0.836	[62]
FeNCP	80 °C	1.50 bar for H_2 and O_2	Cathode contained 1.00 mg cat cm^{-2}, while anode had 0.20 mg Pt cm^{-2}	0.88	[63]
Fe–NC^{BrCl}	80 °C , 100% RH	250 kPa absolute partial pressure H_2 and O_2,	For Fe–NC: 3.5 mg cat cm^{-2} on cathode; for Pt/C: 0.2 mg Pt cm^{-2}, with anode holding 0.4 mg Pt cm^{-2}	1.86	[64]
(Fe,Co)/N-C	80 °C, 100% RH	0.10 Mpa for H_2 and 0.2 Mpa for O_2	0.77 mg cat cm^{-2} placed on cathode; anode contained 0.10 mg Pt cm^{-2}	0.98 (0.2 Mpa O_2)	[65]
Co-N/C-1/4.4	80 °C, 100% RH	1.00/2.00 bar for O_2	Cathode loaded with 3.50 mg cat cm^{-2} and anode with 0.40 mg Pt cm^{-2}	1.12 (2.00 bar O2)	[66]
Fe SAC-MOF-5	80 °C, 100% RH	0.10/0.20 Mpa for O_2	Cathode included 0.10 mg Pt cm^{-2} and anode 0.06 mg Pt cm^{-2}	0.84 (0.20 Mpa)	[67]
OM−Fe−N−C−stea m−800	80 °C, 100% RH	2.00 bar	3.00 mg cat cm^{-2} applied on cathode; 0.10 mg Pt cm^{-2} applied on anode	0.78	[68]
FeSA–N–C	80 °C, 100% RH	1.50 bar	3.00 mg cat cm^{-2}	0.68	[69]
Fe2-Z8-C	80 °C	2.50 bar	2.80 mg cat cm^{-2}	1.141	[70]
OP-Fe-NC	80 °C	2.00 bar	Cathode loading: 4.00 mg cat cm^{-2}; Anode loading: 0.20 mg Pt cm^{-2}	0.937 (2.00 bar)	[71]
Co–N–PCNFs	80 °C, 100% RH	1.00 bar H_2/O_2 /air	4.00 mg cat cm^{-2} assigned to cathode, 0.10 mg Pt cm^{-2} to anode	0.71	[72]

1. *Maximized Fe Utilization*. HRTEM (Fig. 2b, 2d) shows isolated bright atomic features without detectable crystalline Fe by XRD (Fig. 4). This implies that a larger fraction of Fe resides as active Fe–N_x centers rather than as inactive nanoparticles prone to corrosion or agglomeration.
2. *Enhanced Nitrogen Environment*. XPS quantification (Fig. 5b) indicates higher nitrogen content in Fe-N-DPC-1000, which supports the formation and stabilization of Fe–N_x motifs and beneficially tunes their electronic structure for oxygen reduction in acid.
3. *Transport-aware Porosity*. The micro–mesoporous configuration (Fig. 6) couples ~0.55 nm micropores—hosting sites and boosting site density—with ~3.8 nm mesopores, which improve O_2 delivery and water removal. The PVP-free sample, dominated by ~14.6 nm mesopores and lacking strong microporosity, cannot simultaneously ensure high site density and efficient transport.

These features yield improved polarization behavior across the current range and are especially impactful at high current densities, where Fe-N-DPC-1000 sustains higher voltages than Fe-N-C-1000. The reduced mass-transport overpotentials point to fewer diffusion barriers and better water management, confirming that the pore hierarchy functions as designed. In practice, this means that balancing active-site formation with transport pathways translates directly into better single-cell performance.

Conclusion

In brief, our investigation reveals a scalable route for preparing Fe-N-DPC-1000 catalysts using a PVP-assisted MOF synthesis. Adding PVP during precursor formation fundamentally changed the carbonization process. It preserved the framework, enriched nitrogen sites, and promoted highly uniform iron dispersion without forming crystalline byproducts. As a result, the final carbon material retained its polyhedral shape and developed a hierarchical pore structure. Textural analysis confirmed the benefits of this approach. Fe-N-DPC-1000 exhibited a high BET surface area of 1580 $m^2\ g^{-1}$ and a micropore volume of 0.642 $cm^3\ g^{-1}$, providing both a large number of accessible active sites and efficient oxygen pathways.

The performance tests in single-cell PEMFCs further validated the catalyst design. At a cathode loading of only 3 mg cm^{-2}, Fe-N-DPC-1000 achieved a peak power density of 1205 mW cm^{-2}, approximating the Pt/C benchmark while outperforming the PVP-free control by 35.3%. Together, these results highlight PVP-assisted MOF synthesis as a powerful strategy for designing next-generation Fe–N–C catalysts with balanced site density and mass-transport properties. The improved activity was sustained even in the high current density region, where mass transport effects usually dominate, indicating that the dual-scale pore system effectively integrates high site density with unhindered gas accessibility. Enhanced nitrogen incorporation, coupled with the uniform distribution of Fe–N_x centers, contributed to favorable electronic structures and robust turnover frequencies under operating conditions.

Collectively, these findings establish that polymer-assisted MOF engineering is a powerful design strategy for tuning atomic-level coordination, pore hierarchy, and overall catalyst stability in acidic media. The methodology outlined here is not restricted to Fe-based systems and can be applied to other transition-metal–nitrogen–carbon platforms. More broadly, the demonstrated combination of scalability, high activity, and structural

resilience highlights the potential of such catalysts as viable platinum-group-metal-free alternatives. By reducing reliance on scarce noble metals, this approach advances both the technological and environmental dimensions of fuel cell development, aligning with the broader pursuit of sustainable energy conversion.

Acknowledgements

The authors extend their heartfelt thanks to the Sindh Higher Education Commission (SHEC) for supporting this study through project SHEC/SRSP/Engr& Tech/390/2023-24.

Conflict of Interest

The authors declare no conflict of interest.

References

1. M. K. Debe, *Nature*, 486 (2012) 43. https://doi.org/10.1038/nature11115.
2. M. Kiani, Y. Zhao and R. Zhang, *Chem. Commun.*, 61 (2025) 9392. https://doi.org/10.1039/D5CC01478F
3. S. Wang, Y. Chu, C. Lan, C. Liu, J. Ge and W. Xing, *Chem. Synth.*, 3 (2023) 15. https://doi.org/10.20517/cs.2022.36.
4. Q. Meyer, Y. Nie, M. R. Bin Mamtaz and C. Zhao, *ACS Electrochem.,* 1 (2025) 1206. https://doi.org/10.1021/acselectrochem.5c00150.
5. X. Yang, Z. Huang, L. Du, Q. Li and S. Ye, *ACS Catal.*, 14 (2024) 15471. https://doi.org/10.1021/acscatal.4c02871
6. P. Agrawal, S. Ebrahim and D. Ponnamma, *Int. J. Energ. Water Resour.*, 9 (2025) 1005. https://doi.org/10.1007/s42108-024-00324-w.
7. M. A. A. Mohd Nor, M. A. A. Abdul Rani, K. S. Loh, T. F. Choo, K. L. Lim, S. H. Osman, A. C. M. Loy and W. Y. Wong, *J. Power Sour.*, 654 (2025) 237869. https://doi.org/10.1016/j.jpowsour.2025.237869.
8. D. Menga, J. L. Low, Y. -S. Li, I. Arčon, B. Koyutürk, F. Wagner, F. Ruiz-Zepeda, M. Gaberšček, B. Paulus and T. -P. Fellinger, *J. Am. Chem. Soc.,* 143 (2021) 18010. https://doi.org/10.1021/jacs.1c04884.
9. R. Z. Snitkoff-Sol and L. Elbaz, *J. Solid State Electrochem.,* 26 (2022) 1839. https://doi.org/10.1007/s10008-022-05236-5.
10. H. Jin, R. Yu, P. Ji, W. Zeng, Z. Li, D. He and S. Mu, *Chem. Sci.*, 15 (2024) 7259. https://doi.org/10.1039/D4SC01329H
11. H. Xu, R. Li, Y. Li, X. Lu, H. Liu, P. Yang and J. Bai, *J. Mater. Chem. A. Mater.,* 13 (2025) 13675. https://doi.org/10.1039/D5TA01480H
12. K. Kumar, L. Dubau and F. Jaouen, F. Maillard, *Chem. Rev.*, 123 (2023) 9265. https://doi.org/10.1021/acs.chemrev.2c00685.
13. H. Qiu, S. Wen, Q. Fu and X. Zhao, *Catalysts,* 15 (2025) 615. https://doi.org/10.3390/catal15070615.
14. Y. Li, P. Zhang, L. Wan, Y. Zheng, X. Qu, H. Zhang, Y. Wang, K. Zaghib, J. Yuan, S. Sun, Y. Wang, Z. Zhou and S. Sun, *Adv. Funct. Mater.*, 31 (2021) 2009645. https://doi.org/10.1002/adfm.202009645.

15. Q. Lai, L. Zheng, Y. Liang, J. He, J. Zhao and J. Chen, *ACS Catal.*, 7 (2017) 1655. https://doi.org/10.1021/acscatal.6b02966
16. Y. Mao, J. Cheng, H. Guo, L. Qian, J. Tu and W. Yang, *Appl. Surf. Sci.*, 634 (2023) 157679. https://doi.org/10.1016/j.apsusc.2023.157679.
17. L. Wu, R. Zhao, G. Du, H. Wang, M. Hou, W. Zhang, P. Sun and T. Chen, *Green Energ. Environ.*, 8 (2023) 1693. https://doi.org/10.1016/j.gee.2022.03.014.
18. Y. Wu, J. Huang, Z. Lin, L. Li, G. Liang, Y. Qi Jin, G. Huang, H. Zhang, J. Chen, F. Xie, Y. Jin, N. Wang and H. Meng, *Chem. Eng. J.,* 423 (2021) 130241. https://doi.org/10.1016/J.CEJ.2021.130241.
19. K. Li, J. Zhao, R. Yuan, J. Chen, H. Li and X. Wang, *Ionics (Kiel),* 31 (2025) 2021. https://doi.org/10.1007/s11581-024-05990-8.
20. S. Wang, Y. Lv, Y. Yao, H. Yu and G. Lu, *Inorg. Chem. Commun.,* 93 (2018) 56. https://doi.org/10.1016/j.inoche.2018.05.010.
21. J. P. Masnica, S. Sibt-e-Hassan, S. Potgieter-Vermaak, Y. N. Regmi, L. A. King and L. Tosheva, *Green Carbon*, 1 (2023) 160. https://doi.org/10.1016/j.greenca.2023.11.001.
22. J. Xu, G. Liang, D. Chen, Z. Li, H. Zhang, J. Chen, F. Xie, Y. Jin, N. Wang and H. Meng, *Appl. Surf. Sci.,* 573 (2022) 151607. https://doi.org/10.1016/j.apsusc.2021.151607.
23. J. Ma, W. Zhang, F. Yang, Y. Zhang, X. Xu, G. Liu, H. Xu, G. Liu, Z. Wang and S. Pei, *RSC Adv.,* 14 (2024) 4607. https://doi.org/10.1039/D3RA07188J.
24. R. Wang, Y. Wang, Z. Chen, X. Zhong, Y. Xie, X. Ji, J. Liu, S. Xia and Z. Xu, *J. Electrochem. Soc.*, 169 (2022) 060547. https://doi.org/10.1149/1945-7111/ac797f.
25. S. Sabar, A. M. Jamil, Y. Zhao, E.N. MdYusof, R. Schneider, A.R. Mohamed, Y. Kuwahara, K. Mori and H. Yamashita, *New J. Chem.,* 49 (2025) 8267. https://doi.org/10.1039/D5NJ00407A
26. W. Wang, J. Luo, W. Chen, J. Li, W. Xing and S. Chen, *J. Mater. Chem. A Mater*, 4 (2016) 12768. https://doi.org/10.1039/C6TA05075A
27. Z. Luo, T. Zhou, Y. Guan, L. Zhang, Q. Zhang, C. He, X. Sun and X. Ren, *Small,* 19 (2023) 2304750. https://doi.org/10.1002/smll.202304750.
28. Y. He and G. Wu, *Acc. Mater. Res.,* 3 (2022) 224. https://doi.org/10.1021/accountsmr.1c00226.
29. Q. Xue, X. Qi, K. Li, Y. Zeng, F. Xu, K. Zhang, X. Qi, L. Li and A. Cabot, *RSC Adv*., 14 (2024) 16379. https://doi.org/10.1039/D4RA01754D.
30. X. Shu, X. Cao, B. He, X. Chen, L. Zhao, C. Yang, J. Ma and J. Zhang, *Energ. Environ. Sci.,* 18 (2025) 1262. https://doi.org/10.1039/D4EE04465G
31. J. Liu, W. Chen, S. Yuan, T. Liu and Q. Wang, *Energ. Environ. Sci.*, 17 (2024) 249. https://doi.org/10.1039/D3EE03183G

32. Y. Zhou, R. Lu, X. Tao, Z. Qiu, G. Chen, J. Yang, Y. Zhao, X. Feng and K. Müllen, *J. Am. Chem. Soc.,* 145 (2023) 3647. https://doi.org/10.1021/jacs.2c12933.
33. C. Shao, L. Wu, H. Zhang, Q. Jiang, X. Xu, Y. Wang, S. Zhuang, H. Chu, L. Sun, J. Ye, B. Li and X. Wang, *Adv. Funct. Mater.,* 31 (2021) 2100833. https://doi.org/10.1002/adfm.202100833.
34. F. Zhang, Y. Chen, Y. Liu, X. Liu and S. Gao, *Int. J. Hydrogen Energ.*, 46 (2021) 37895. https://doi.org/10.1016/j.ijhydene.2021.09.040.
35. N. He, W. Li, T. Shi, Z. Li, F. Guo, Z. Li and X. Zhao, *ACS Appl. Polym. Mater.,* 6 (2024) 2814. https://doi.org/10.1021/acsapm.3c03026.
36. K. M. Koczkur, S. Mourdikoudis, L. Polavarapu and S.E. Skrabalak, *Dalton Trans.,* 44 (2015) 17883. https://doi.org/10.1039/C5DT02964C
37. J. L. Chen, W. B. Li and B. Q. Xu, *J. Colloid Interf. Sci.,* 502 (2017) 44. https://doi.org/10.1016/j.jcis.2017.04.012.
38. F. Zhang, J. Zhang, J. Ma, X. Zhao, Y. Li and R. Li, *J. Colloid Interf. Sci.,* 593 (2021) 32. https://doi.org/10.1016/J.JCIS.2021.02.101.
39. J. Zhang, Q. Li, I.S. Amiinu, H. Wu, C. Zhang, K. Cheng, H. Zhou and S. Mu, *Electrochim. Acta,* 177 (2015) 73. https://doi.org/10.1016/j.electacta.2015.01.172.
40. Z. Qiu, N. Huang, X. Ge, J. Xuan and P. Wang, *Int. J. Hydrogen Energ.*, 45 (2020) 8667. https://doi.org/10.1016/j.ijhydene.2020.01.112.
41. X. Zhang and L. Wu, *Ionics* (Kiel), 28 (2022) 3435. https://doi.org/10.1007/s11581-022-04581-9.
42. M. Shoaib, S. Ishtiaque, A.A. Ghani, Z. Awan, A. Ali, A. Rubab and M. Akhtar, *RSC Adv.,* 15 (2025) 34524. https://doi.org/10.1039/D5RA05653E
43. I. Martinaiou and M. K. Daletou, *Energies (Basel),* 17 (2024) 3443. https://doi.org/10.3390/en17143443.
44. F. Liu, L. Shi, X. Lin, B. Zhang, Y. Long, F. Ye, R. Yan, R. Cheng, C. Hu, D. Liu, J. Qiu and L. Dai, *Sci. Adv.,* 9 (2023) eadg0366. https://doi.org/10.1126/sciadv.adg036
45. F. Liu, L. Shi, X. Lin, D. Yu, C. Zhang, R. Xu, D. Liu, J. Qiu and L. Dai, *Appl. Catal. B.,* 302 (2022) 120860. https://doi.org/10.1016/j.apcatb.2021.120860.
46. Y. Wu, M. Yuan, X. Li, R. Ding, X. Duan, J. Li, Y. Wang, X. Li, Y. Zhang and J. Liu, *Appl. Catal. B.,* 312 (2022) 121365. https://doi.org/10.1016/j.apcatb.2022.121365.
47. Y. Guo, L. Feng, C. Wu, X. Wang and X. Zhang, *J. Catal.*, 390 (2020) 213. https://doi.org/10.1016/j.jcat.2020.07.037.
48. X. Guo, H. Xu, W. Li, Y. Liu, Y. Shi, Q. Li and H. Pang, *Adv. Sci.*, 10 (2023) 2206084. https://doi.org/10.1002/advs.202206084.
49. L. Yang, D. Cheng, H. Xu, X. Zeng, X. Wan, J. Shui, Z. Xiang and D.

Cao, *Proc. Nat. Acad. Sci.,* 115 (2018) 6626. https://doi.org/10.1073/pnas.1800771115.
50. Y. Zhang, Y. Jia, M. Li and L. Hou, *Sci. Rep.,* 8 (2018) 9597. https://doi.org/10.1038/s41598-018-28015-7.
51. Y. Pan, Y. Liu, G. Zeng, L. Zhao and Z. Lai, *Chem. Commun.*, 47 (2011) 2071. https://doi.org/10.1039/c0cc05002d.
52. A. Schejn, L. Balan, V. Falk, L. Aranda, G. Medjahdi and R. Schneider, *Cryst. Eng. Comm.,* 16 (2014) 4493. https://doi.org/10.1039/C3CE42485E
53. K. S. Park, Z. Ni, A. P. Côté, J. Y. Choi, R. Huang, F.J. Uribe-Romo, H. K. Chae, M. O'Keeffe and O.M. Yaghi, *Proc. Natl. Acad. Sci. U.S.A.*, 103 (2006) 10186. https://doi.org/10.1073/pnas.0602439103.
54. S. Zhang, B. Sun, K. Liao, X. Wang, Z. Chen, J. Wang, W. Hu and X. Han, *Adv. Funct. Mater.*, 35 (2025) 2425640. https://doi.org/10.1002/adfm.202425640.
55. Y. Jia, C. Shi, W. Zhang, W. Xia, M. Hu, R. Huang and R. Qi, *Nanomaterials*, 12 (2022) 1593. https://doi.org/10.3390/nano12091593.
56. O.S. Oluwole, P. Jovanović, S.C. Mohonta, T.K. Nguyen, P. Aitchison, N. C. Karmakar and M. Majumder, *Mater. Appl.,* 9 (2025) 52. https://doi.org/10.1038/s41699-025-00572-2.
57. L. Li, Y. Wen, G. Han, Y. Liu, Y. Song, W. Zhang, J. Sun, L. Du, F. Kong, Y. Ma, Y. Gao, J. Wang, C. Du and G. Yin, *Chem. Eng. J.,* 437 (2022) 135320. https://doi.org/10.1016/j.cej.2022.135320.
58. R. Zhang, T. Liu, W. Li, Z. Ma, P. Pei, W. Zhang, K. Yang and Y. Tao, *J. Nanobiotechnol.,* 20 (2022) 223. https://doi.org/10.1186/s12951-022-01442-5.
59. A. El Nemr, R.M. Aboughaly, A. El Sikaily, S. Ragab, M. S. Masoud and M.S. Ramadan, *Biomass Convers. Biorefin.,* 13 (2023) 1581. https://doi.org/10.1007/s13399-021-01445-6.
60. S. Kute, M. Pandey and M. Zate, *Discov. Electron.*, 2 (2025) 57. https://doi.org/10.1007/s44291-025-00094-7.
61. Z. Guo, Z. Zhang, Z. Li, M. Dou and F. Wang, *Nano Energ.*, 57 (2019) 108. https://doi.org/10.1016/j.nanoen.2018.12.009.
62. C. Liu, J. Zheng, B. Chi, C. Zhong, Y. Deng, C. Chen, D. Dang, W. Fan, Z. Cui and Q. Liu, *Energ. Environ. Sci.,* 17 (2024) 5941. https://doi.org/10.1039/D4EE00493K
63. J. Roh, A. Cho, S. Kim, K.-S.Lee, J. Shin, J.S. Choi, J. Bak, S. Lee, D. Song, E.-J.Kim, C. Lee, Y.R. Uhm, Y.-H.Cho, J.W. Han and E. Cho, *ACS Catal.,* 13 (2023) 9427. https://doi.org/10.1021/acscatal.3c01136
64. S. Yin, L. Chen, J. Yang, X. Cheng, H. Zeng, Y. Hong, H. Huang, X. Kuai, Y. Lin, R. Huang, Y. Jiang and S. Sun, *Nat. Commun.*, 15 (2024) 7489. https://doi.org/10.1038/s41467-024-51858-w.

65. J. Wang, Z. Huang, W. Liu, C. Chang, H. Tang, Z. Li, W. Chen, C. Jia, T. Yao, S. Wei, Y. Wu and Y. Li, *J. Am. Chem. Soc.,* 139 (2017) 17281. https://doi.org/10.1021/jacs.7b10385.
66. X.-M. Qu, S.-H.Yin, Y.-N.Yan, J. Yang, Y.-R.Li, X.-Y.Cheng, F. Lu, C.-T.Wang, Y.-X.Jiang and S.-G.Sun, *Chem. Eng. J.*, 461 (2023) 142054. https://doi.org/10.1016/j.cej.2023.142054.
67. X. Xie, L. Shang, X. Xiong, R. Shi and T. Zhang, *Adv. Energ. Mater.*, 12 (2022) 2102688. https://doi.org/10.1002/aenm.202102688
68. J. Zou, C. Chen, Y. Chen, Y. Zhu, Q. Cheng, L. Zou, Z. Zou and H. Yang, *ACS Catal.,* 12 (2022) 4517. https://doi.org/10.1021/acscatal.2c00408
69. L. Jiao, R. Zhang, G. Wan, W. Yang, X. Wan, H. Zhou, J. Shui, S.-H. Yu and H.-L.Jiang, *Nat. Commun.*, 11 (2020) 2831. https://doi.org/10.1038/s41467-020-16715-6.
70. Q. Liu, X. Liu, L. Zheng and J. Shui, *Angew. Chem. Int. Ed.*, 57 (2018) 1204. https://doi.org/10.1002/anie.201709597.
71. J. Li, W. Xia, X. Xu, D. Jiang, Z.-X. Cai, J. Tang, Y. Guo, X. Huang, T. Wang, J. He, B. Han and Y. Yamauchi, *J. Am. Chem. Soc*., 145 (2023) 27262. https://doi.org/10.1021/jacs.3c05544.
72. Y. He, H. Guo, S. Hwang, X. Yang, Z. He, J. Braaten, S. Karakalos, W. Shan, M. Wang, H. Zhou, Z. Feng, K.L. More, G. Wang, D. Su, D.A. Cullen, L. Fei, S. Litster and G. Wu, *Adv. Mater.*, 32 (2020) 2003577. https://doi.org/10.1002/adma.202003577.